INTERNATIONAL JOURNAL FOR NUMERICAL METHODS IN FLUIDS, VOL. 11, 227–245 (1990)

A COMPREHENSIVE ANALYSIS OF THE VISCOUS INCOMPRESSIBLE FLOW IN QUASI-THREE-DIMENSIONAL AEROFOIL CASCADES

E. A. BASKHARONE AND D. R. McARTHUR

Department of Mechanical Engineering, Texas A&M University, College Station, TX 77843, U.S.A.

SUMMARY

A rigorous model of the fully elliptic flow over the blade-to-blade stream surface in an annular aerofoil cascade is developed. The model accuracy stems from its precise simulation of the meridional hub-to-casing flow effects, including those of the shear stress components that are created by the spanwise velocity gradients. These stresses are unprecedentedly introduced in the flow-governing equations in the form of source terms and are modelled as such. The final set of flow-governing equations are solved using the Galerkin weighted residual method coupled with a biquadratic finite element of the Lagrangian type. The flow solution is verified against the numerical results of a fully three-dimensional flow model and a set of experimental data, both concerning a low-aspect-ratio stator of an axial flow turbine under a low Reynolds number and subsonic flow operation mode. The numerical results in this case show well predicted aerofoil loading and pitch-averaged exit flow conditions. Also evident is a substantial capability of the analysis in modelling such critical regions as the wake subdomain. It is further proven that the new terms in the governing equations enhance the quality of the numerical predictions in this class of flow problems.

KEY WORDS Quasi-three-dimensional flow Aerofoil cascades Meridional/Blade-to-blade flow interaction

1. INTRODUCTION

A growing effort is being devoted to the improvement of bladed component efficiency in gas turbine engines towards an optimum overall performance. Considering the high cost of experimentation in this area, computational models have progressively been developed with the hope of reliably predicting the flow behaviour in annular aerofoil cascades. Conceptually, the problem is that of a three-dimensional periodic flow in the blade-to-blade, hub-to-casing passage of a turbomachine. In modelling this flow type it is crucial to account for such effects as flow recirculation, trailing edge mixing and wake structure. Existing numerical models in this area vary in complexity from the potential flow category[1–3] to that of viscous flow.[4,5] Compared to strictly two- and three-dimensional flow models, the quasi-three-dimensional approach to the cascade flow problem has been recognized as a sensible compromise in aspects of both economy and precision. It is, however, the viscous flow version of the problem under this approach that is in need of further enhancement, particularly in the area of simulating the hub-to-casing/blade-to-blade flow interaction effects.

Existing viscous flow models of aerofoil cascades can be classified into two major categories: one of simple analyses and various levels of uncertainty, and another category of full-scale models

0271–2091/90/100227–19$09.50

Received 5 December 1988
Revised 19 October 1989

with undesirably high requirements of computational resources. Of these, the first category includes strictly two-dimensional (e.g. Reference 4) and quasi-three-dimensional (e.g. References 5–7) flow models. A common feature here is that ellipticity of the viscous flow field in this case is either partially or totally ignored. The most recent of these models generally employ the thin-layer approximation[4,6,7] whereby different levels of inviscid/viscous flow interaction are introduced in an attempt to partially simulate the elliptic nature of the flow field. Another common feature is that the flow passage is defined as bounded by two successive mid-channel streamlines (of the type shown in Figure 3), which are computed on an inviscid flow basis and are later treated as flow non-permeable in the viscous flow phase of the computational procedure. It is, however, the extraction of the streamwise diffusion terms from the viscous flow equations that is, in the majority of these models, most damaging, since it unjustifiably forbids the downstream effects from influencing the flow behaviour. Under such an assumption, and with the exception of the exit pressure which is externally fixed, the flow exit conditions are normally obtained by extrapolation[6,7] and are generally inaccurate, at least from an analytical standpoint. The category of complex flow models, on the other hand, is best represented by that of Hah,[8] in which the ellipticity of the flow-governing equations is maintained throughout the computational domain. However, in view of the complex nature of the blade-to-blade, hub-to-casing flow passage in this case, the passage geometry in Hah's model was considerably simplified. The blade in this model is in fact assumed to be untwisted, unleaned and untitled in the spanwise direction, and the aerofoil geometry is restricted to being identical at all radial locations. These simplifications, which are hardly applicable to modern turbine blades, had nevertheless no appreciable effect on the size of the computational model, which was exceedingly large. As a result, utilization of such a flow model in a normal design process, especially in its preliminary phase, would be unwise. Other existing models of the three-dimensional flow type are commonly based on the parabolized flow principle (e.g. References 9 and 10) and are conceptually less accurate by comparison.

The present model fits under the quasi-three-dimensional flow models but deviates from existing models in the aspects of accuracy and completeness. The idea here is to iteratively solve the flow over two families of orthogonal stream surfaces (Figure 1) and was devised by Wu[11] for a rotational, yet inviscid, cascade flow. Unfortunately, existing blade-to-blade flow models (e.g. References 5–7), which were aimed at extending Wu's theory to viscous flow computations, have commonly ignored the viscosity-related stresses on the blade-to-blade stream surface that would, according to Wu's procedure, be the outcome of the meridional (hub-to-casing) flow computational phase. Examination of the flow-governing equations in these models also revealed that other, but perhaps less damaging, approximations have traditionally been introduced. The starting point in this study was therefore a rigorous derivation of the flow-governing equations in their most general form by applying the basic conservation principles to the typical fluid element shown in Figure 2. Among the differences between the final set of equations and those in the standard formulation is a term that is proportional to the second streamwise derivatives of the stream tube thickness b and the radius r (Figure 2), as well as a key term through which the shear stresses (identified by double arrowheads in Figure 2) over the upper and lower surfaces of the control volume are introduced in the equations of motion. Disappearance of the former term from the standard equations is a result of treating b and/or r as linear functions of the meridional distance s (e.g. Reference 5), which is often a restrictively fictitious assumption. This is true in the sense that b is primarily dependent on the endwall contours, which are often made non-linear in an attempt by the designer to alleviate excessive diffusion along the blade suction side. On the other hand, ignoring the above mentioned shear stress components, which are generated by the local spanwise gradients of the meridional and tangential velocity components, implies a hub-to-casing free vortex flow behaviour which is simply inconsistent with recent gas turbine design trends, particularly in the propulsion area. The desire to minimize the weight and maximize the power in this gas turbine area often leads to low-aspect-ratio bladings with spanwise stacking patterns that are highly non-uniform (Figure 4). These complex patterns, added to typically significant spanwise variations of the aerofoil setting angles, create high spanwise velocity gradients which in turn produce the shear stress components on the stream tube inner and outer surfaces. The accuracy imparted to the computational model through refinement of the flow equations is, on the other hand, preserved by maintaining the flow ellipticity throughout the computational domain. As a result, the built-in capability of the governing equations to predict such loss-generating mechanisms as separation, recirculation and near-wake mixing is uncompromised.

2. ANALYSIS

Different views of the computational domain under consideration are shown in Figure 1. The meridional view of the domain shows radius and stream tube thickness variations which are totally unrestricted. Arbitrariness of these two parameters makes the current flow model applicable to general bladed components of turbomachines regardless of the meridional shape of the flow passage.

It is assumed that the meridional view of the blade-to-blade stream tube (Figure 1) is readily defined. This is normally achievable through any of the existing axisymmetric flow codes (e.g. Reference 12). It is worth noting, however, that even the simple codes frequently used in the gas turbine industry for this purpose (e.g. References 13 and 14) normally account, to a good extent and through implicit means, for different real flow effects such as the blade blockage and profile losses, both of which are functions of the spanwise location. As a result, the spanwise velocity gradients produced by these codes are typically significant and highly representative of real flow effects in the meridional plane. These are the same gradients used in the current model to compute the shear stress components over the inner and outer stream tube surfaces (Figure 2). Applicable assumptions in the present model also include a steady, adiabatic and laminar flow through the aerofoil cascade. Of these, the laminar flow assumption confines the model applicability to operation modes with sufficiently low Reynolds numbers (typically below 2×10^5). In spite of the apparent limitations that are implied by such an assumption, the choice here was in part motivated by the desire to extract the inaccuracy associated with what would have realistically been a low-order turbulence closure (e.g. Reference 7), concentrating instead on the manner in which refinement of the flow equations impacts the laminar flow field in a representative cascade, which is the main thrust of this study.

2.1. *Flow-governing equations*

Detailed derivation of these equations in their most general form is provided in the Appendix with reference to the fluid element in Figure 2. Although the equations are derived for a stationary blade row, the Appendix also contains definitions of the additional terms, such as those created by the Coriolis and centrifugal acceleration components in the case of a rotor cascade, for the purpose of completeness. Yet one of the fundamental differences between these and the traditional equations in any of similar existing models is that the shear forces on the fluid element faces below and above the mean stream surface (Figure 2) are now taken into account. These forces, as seen in the Appendix, are proportional to the spanwise gradients of velocity components, which, as indicated earlier, are viewed as a partial outcome of the preprocessing phase that involves the hub-to-casing axisymmetric flow field.

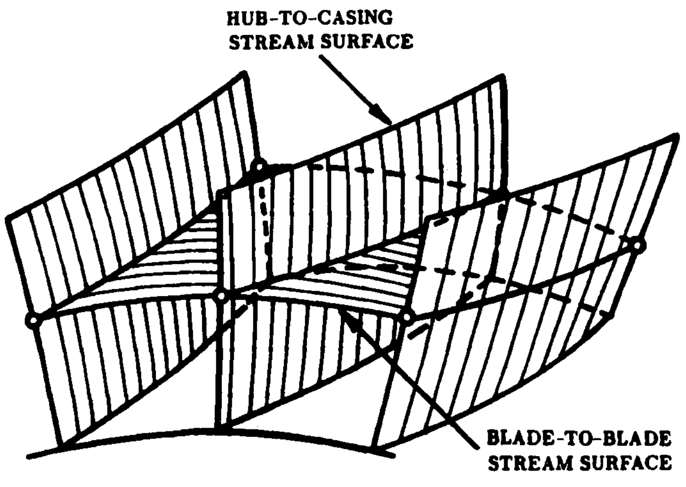

ARRANGEMENT OF WU'S STREAM SURFACES

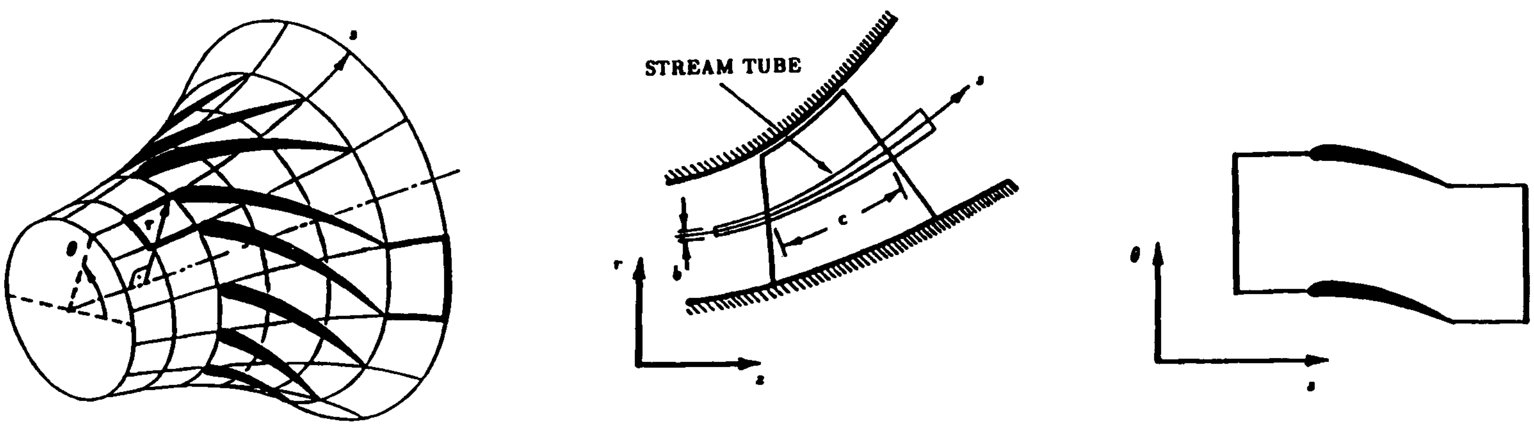

ISOMETRIC VIEW OF THE
BLADE-TO-BLADE STREAM SURFACE

MERIDIONAL PROJECTION

BLADE-TO-BLADE PROJECTION

Figure 1. Definition of the computational domain

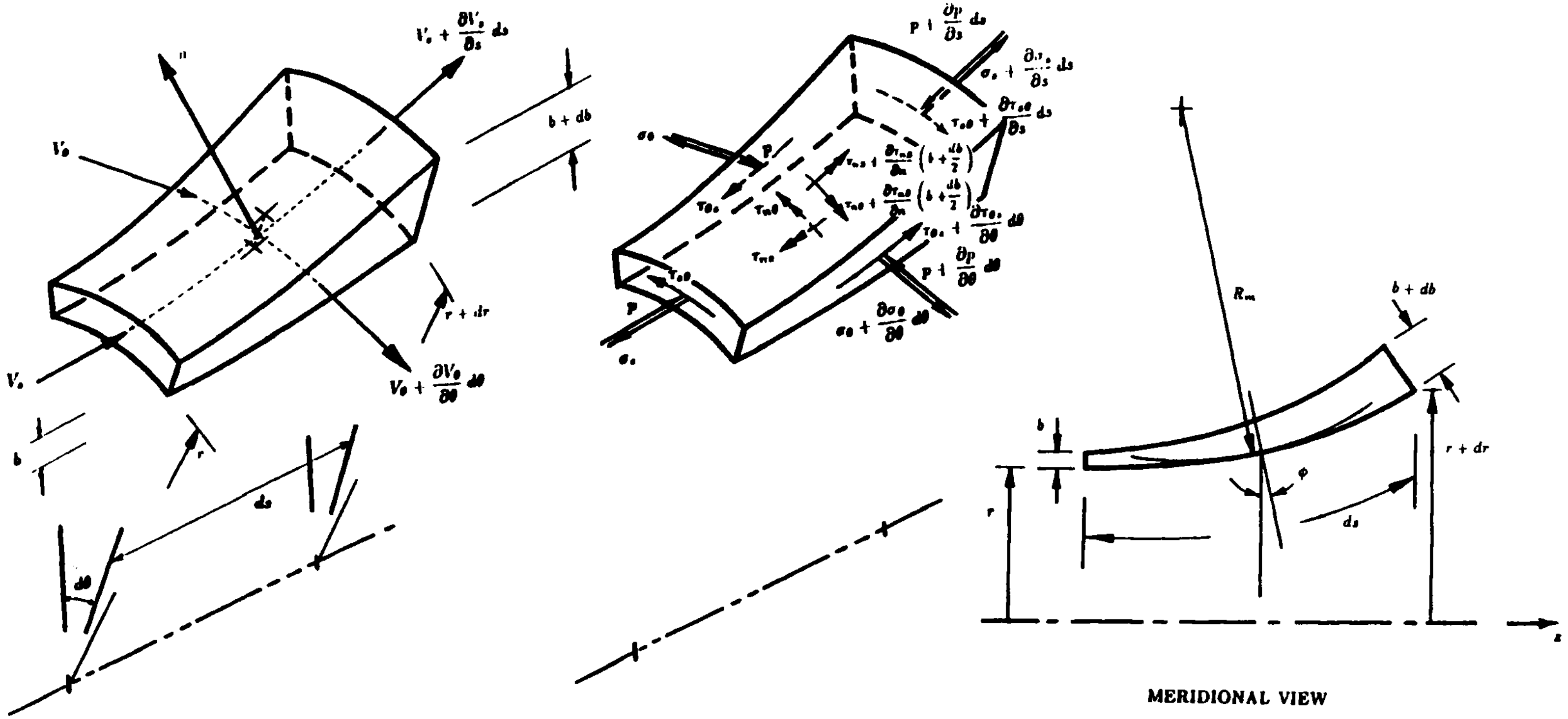

Figure 2. Velocity and stress patterns on a quasi-three-dimensional fluid element

In their final form, the mass and momentum conservation equations can be expressed as follows:

$$\frac{1}{b}\frac{\partial}{\partial s}(rbV_s)+\frac{\partial V_\theta}{\partial \theta}=0, \tag{1}$$

$$\nu\nabla^2 V_s=\frac{1}{\rho}\left(\frac{1}{b}\frac{\mathrm{d}b}{\mathrm{d}s}+\frac{1}{r}\frac{\mathrm{d}r}{\mathrm{d}s}\right)p+\frac{1}{\rho}\frac{\partial p}{\partial s}+\alpha_1\frac{\partial V_s}{\partial s}+\alpha_2\frac{\partial V_s}{\partial \theta}+\alpha_3 V_s+\alpha_4 V_\theta+\alpha_5, \tag{2}$$

$$\nu\nabla^2 V_\theta=\frac{1}{\rho r}\frac{\partial p}{\partial \theta}+\beta_1\frac{\partial V_\theta}{\partial s}+\beta_2\frac{\partial V_\theta}{\partial \theta}+\beta_3 V_\theta+\beta_4\frac{\partial V_s}{\partial \theta}+\beta_5 V_s+\beta_6, \tag{3}$$

where the coefficients α_1–α_5 and β_1–β_6 are defined in the Appendix. The contents of these coefficients is where the newly introduced flow effects present themselves. Besides, the appearance of the first term on the right-hand side of equation (2) is a result of radius and stream tube thickness variations and is also an aspect in which the current equations differ from those in the literature.

2.2. Boundary conditions

In an elliptic flow model the solution is highly sensitive to the prescribed flow behaviour over the different boundary segments. Of these, the periodic and exit boundaries (Figure 3) are largely within the wake, where an artificially imposed flow pattern can lead to severe inaccuracies.

The flow exit boundary conditions are based on the assumption that the exit station is located sufficiently far from the aerofoil trailing edge for a nearly complete mixing of the suction- and pressure-side streams. In this case the exit flow behaviour is dictated by the following Neumann-type boundary conditions:

$$\frac{\partial V_s}{\partial s}=-\frac{V_s}{rb}\frac{\mathrm{d}}{\mathrm{d}s}(rb), \tag{4}$$

$$\frac{\partial V_\theta}{\partial s}=-\frac{V_\theta}{r}\frac{\mathrm{d}r}{\mathrm{d}s}, \tag{5}$$

where V_s and V_θ are the velocity components (Figure 2), r is the local radius and b is the local stream tube thickness. Equation (4) is recognized as a special form of the continuity equation in the Appendix, while equation (5) is a general derivative-type version of the angular momentum conservation principle which would, with reasonable accuracy, prevail at this far-downstream location. It is seen that the exit flow behaviour in the current analysis is unrestricted to artificially satisfy any uniform distribution of, for instance, the exit flow direction. Also note that the special geometrical features of the meridional view of the solution domain (Figure 1) make it inappropriate to specify any relatively simple exit conditions, such as zero surface tractions, since this would be incompatible with, for instance, the stream tube thickness variation as the exit station is approached.

The cascade periodicity in the current analysis is implicitly enforced in a manner that eliminates abrupt changes in the field variables across the periodic boundaries while minimizing the core size during execution. Here, corresponding nodes on a pair of periodic boundaries are assigned the same global degree of freedom in the finite element model. In this case, contributions from finite elements sharing both nodes appear in the final form of the finite element equations associated with this degree of freedom.

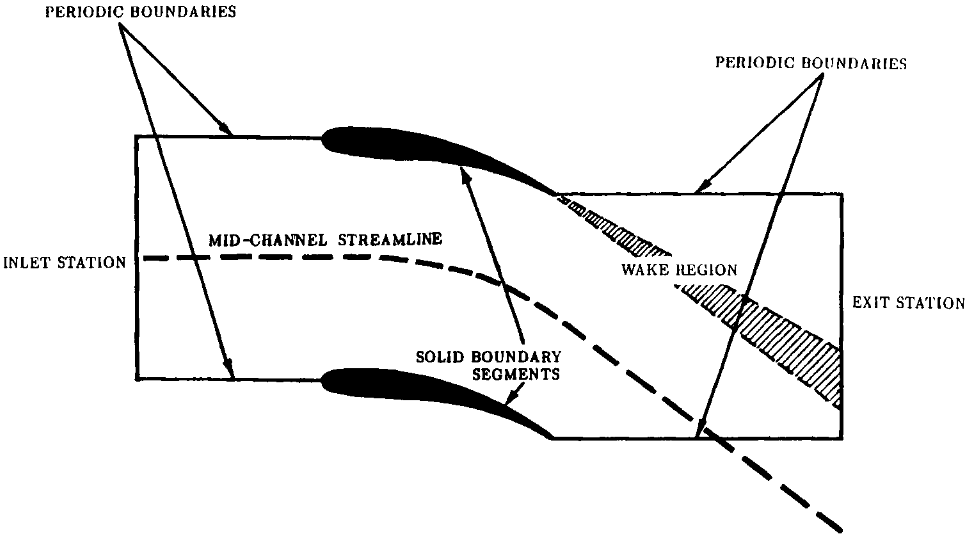

Figure 3. Types of boundary conditions

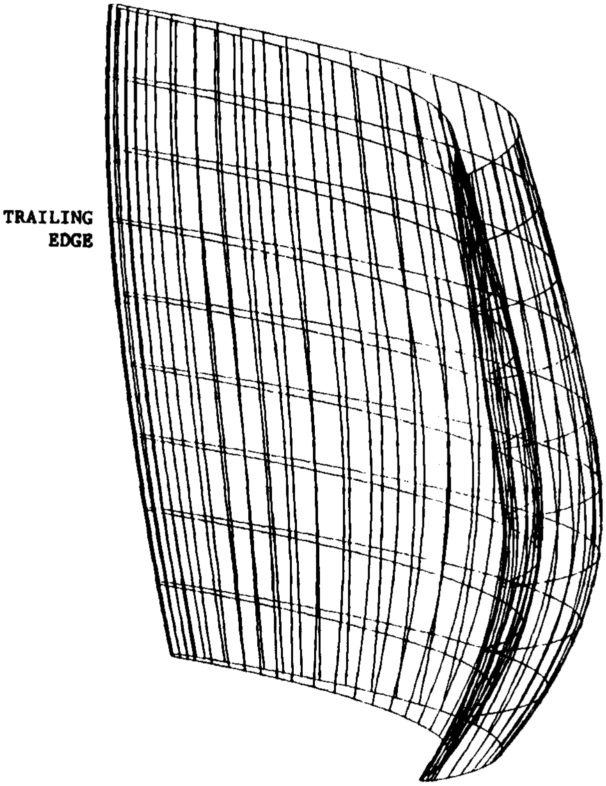

Figure 4. Typical aerofoil stacking pattern of a low-aspect-ratio gas turbine stator

Other applicable boundary conditions involve the remaining boundary segments and are all of the Dirichlet type. At the inlet station, both the through-flow and tangential velocity components, V_s and V_θ, are specified in accordance with the cascade operating conditions. Furthermore, the static pressure is fixed at the exit station and the no-slip condition is imposed over the aerofoil surface.

2.3. *Finite element formulation*

In the following a Bubnov–Galerkin finite element formulation of the flow-governing equations is developed, with the discretization unit being a biquadratic curve-sided finite element of the Lagrangian type. Figure 5 shows this nine-noded element which was proven[15] to be highly accurate in the current 'primitive variables' form the Navier–Stokes equations. Elemental interpolation of the flow variables, on the other hand, is established in such a manner as to ensure satisfaction of the Ladyzhenskaya–Babuška–Brezzi compatibility requirements.[16,17] Applied to the current problem, these requirements give rise to a subfamily of velocity/pressure interpolation combinations under which a stable and convergent solution is achievable.

Throughout a typical element e let the velocity components and static pressure be interpolated as follows:

$$V_s^{(e)} = \sum_{i=1}^{9} N_i V_{s,i}, \tag{6}$$

$$V_\theta^{(e)} = \sum_{i=1}^{9} N_i V_{\theta,i}, \tag{7}$$

$$p^{(e)} = \sum_{k=1}^{4} M_k p_k, \tag{8}$$

where N_i is a quadratic 'shape' function of the local co-ordinates ζ and η that is associated with the ith corner, midside or interior node of the element in the local frame of reference,[17] M_k is a linear function of ζ and η that is associated with the kth corner node of the element, and $V_{s,i}$, $V_{\theta,i}$ and p_k are the nodal values of velocity components and pressure.

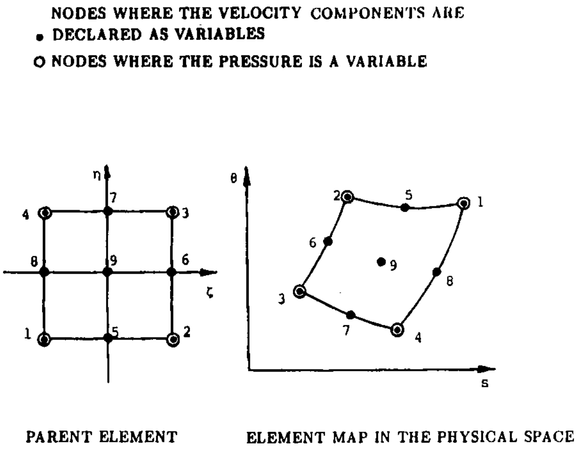

Figure 5. Quadratic curve-sided finite element of the Lagrangian type

The physical co-ordinates s and θ are also mapped into the local frame of reference as follows:

$$s=\sum_{i=1}^{9} N_i s_i, \tag{9}$$

$$\theta=\sum_{i=1}^{9} N_i \theta_i. \tag{10}$$

Application of the Bubnov–Galerkin method[17] in this case gives rise to the following set of equations for the typical finite element:

continuity equation

$$A_{kj}V_{s,j}+B_{kj}V_{\theta,j}=0, \tag{11}$$

s-momentum equation

$$C_{ij}V_{s,j}+D_{ij}V_{\theta,j}+E_{ik}p_k=I_{s,i}, \tag{12}$$

θ-momentum equation

$$F_{ij}V_{s,j}+G_{ij}V_{\theta,j}+H_{ik}p_k=I_{\theta,i}. \tag{13}$$

Here

$$A_{kj}=\int_{-1}^{+1}\int_{-1}^{+1}|J|rM_k\left(br\frac{\partial N_j}{\partial s}+N_j\frac{\mathrm{d}(br)}{\mathrm{d}s}\right)\mathrm{d}\zeta\mathrm{d}\eta,$$

$$B_{kj}=\int_{-1}^{+1}\int_{-1}^{+1}|J|brM_k\frac{\partial N_j}{\partial\theta}\mathrm{d}\zeta\mathrm{d}\eta,$$

$$C_{ij}=\int_{-1}^{+1}\int_{-1}^{+1}|J|br\left[\nu\left(\frac{\partial N_i}{\partial s}\frac{\partial N_j}{\partial s}+\frac{1}{r^2}\frac{\partial N_i}{\partial\theta}\frac{\partial N_j}{\partial\theta}\right)+\alpha_1N_i\frac{\partial N_j}{\partial s}+\alpha_2N_i\frac{\partial N_j}{\partial\theta}+\alpha_3N_iN_j\right]\mathrm{d}\zeta\mathrm{d}\eta,$$

$$D_{ij}=\int_{-1}^{+1}\int_{-1}^{+1}|J|br\alpha_4N_iN_j\mathrm{d}\zeta\mathrm{d}\eta,$$

$$E_{ij}=\int_{-1}^{+1}\int_{-1}^{+1}\frac{1}{\rho}|J|br\left[N_i\frac{\partial M_k}{\partial s}+\left(\frac{1}{b}\frac{\mathrm{d}b}{\mathrm{d}s}+\frac{1}{r}\frac{\mathrm{d}r}{\mathrm{d}s}\right)N_iM_k\right]\mathrm{d}\zeta\mathrm{d}\eta,$$

$$I_{s,i}=\oint_{l^{(e)}}\nu N_i\frac{\partial V_s}{\partial\mathbf{n}}\mathrm{d}l-\int_{-1}^{+1}\int_{-1}^{+1}|J|brN_i\alpha_5\mathrm{d}\zeta\mathrm{d}\eta,$$

$$F_{ij}=\int_{-1}^{+1}\int_{-1}^{+1}|J|br\left(\beta_4N_i\frac{\partial N_j}{\partial\theta}+\beta_5N_iN_j\right)\mathrm{d}\zeta\mathrm{d}\eta,$$

$$G_{ij}=\int_{-1}^{+1}\int_{-1}^{+1}|J|br\left[\nu\left(\frac{\partial N_i}{\partial s}\frac{\partial N_j}{\partial s}+\frac{1}{r^2}\frac{\partial N_i}{\partial\theta}\frac{\partial N_j}{\partial\theta}\right)+\beta_1N_i\frac{\partial N_j}{\partial s}+\beta_2N_i\frac{\partial N_j}{\partial\theta}+\beta_3N_iN_j\right]\mathrm{d}\zeta\mathrm{d}\eta,$$

$$H_{ik}=\int_{-1}^{+1}\int_{-1}^{+1}\frac{1}{\rho r}|J|bN_i\frac{\partial M_k}{\partial\theta}\mathrm{d}\zeta\mathrm{d}\eta,$$

$$I_{\theta,i}=\oint_{l^{(e)}}\nu N_i\frac{\partial V_\theta}{\partial\mathbf{n}}\mathrm{d}l-\int_{-1}^{+1}\int_{-1}^{+1}|J|brN_i\beta_6\mathrm{d}\zeta\mathrm{d}\eta,$$

where $|J|$ is the Jacobian of co-ordinate transformation, $I_{s,i}$ and $I_{\theta,i}$ are closed integrals performed along the element boundary and $\mathbf{n}$ is the outward unit vector normal to the element boundary

(Figure 2), with α_1–α_5 and β_1–β_6 being those defined in the Appendix. Note that the double integrals appearing in the $I_{s,i}$ and $I_{\theta,i}$ expressions (above) result from the shear stresses over the inner and outer surfaces of the fluid element (Figure 2), which are treated as source terms. This becomes clear by examination of the expressions for α_5 and β_6 in the Appendix. The assembled set of finite element equations are stored in partially packed arrays in order to reduce the core requirement and are subsequently solved using the numerical procedure by Gupta and Tanji,[18] which is based on the Gauss–Jordan elimination technique.

2.4. Method of numerical solution

The flow solution is obtained iteratively through progressively updating the functions $\hat{V}_s$ and $\hat{V}_\theta$ in the momentum equations (see Appendix) in a successive substitution fashion. The computational procedure in this case is initialized by solving the flow equations for a theoretically creeping flow. The resulting velocity field is then used to upgrade the finite element equations and the process repeated towards conversion. This inner loop is re-entered within an outer loop in which the Reynolds number is elevated by equal increments of 500. An underrelaxation factor varying from 0·6 to 0·8 was used to ensure monotonic convergence.

The state of numerical convergence was defined to occur whenever the summation of non-dimensionalized error in any of the flow variables, namely the velocity components and pressure, over all nodal points maintained a sufficiently small value in two consecutive iterations, i.e.

$$\sum_i \left| \frac{\phi_i^{(n)} - \phi_i^{(n-1)}}{\phi_i^{(n)}} \right|^2 < \varepsilon,$$

$$\sum_i \left| \frac{\phi_i^{(n-1)} - \phi_i^{(n-2)}}{\phi_i^{(n-1)}} \right|^2 < \varepsilon,$$

where ϕ_i refers to the ith nodal value of a velocity component or static pressure, n is the iterative step at convergence and ε is a tolerance factor set to be 3%.

The reason for invoking two successive numerical solutions in the convergence criterion was to provide a means for differentiating between the state of actual convergence and that of numerical fluctuation. It was generally observed that the error jumps abruptly and a state of numerical oscillation occurs once the Reynolds number is elevated. This state again prevailed, but at much lower error levels, near the iterative step where convergence was finally achieved.

3. RESULTS AND DISCUSSION

A test case involving the mean section of a contoured endwall, low-aspect-ratio stator of a gas turbine was selected for the purpose of code verification. The stator flow measurements[19,20] correspond to a 2·6:1 scaled-up version of the original design and reflect a low-pressure-ratio operation mode with an exit critical velocity ratio of 0·3, for which the flow is incompressible for all practical purposes. Moreover, the low subsonic flow in the stator passages in this case gave rise to a low Reynolds number which, together with the flow incompressibility, is consistent with the assumptions made in the current study.

Figures 6 and 7 show the turbine stator section under consideration and the blade-to-blade finite element discretization model. As seen in Figure 6, the section is one where both the radius and stream tube thickness are generally functions of the meridional distance, which was a desired feature in the test case selection process. Another motivating feature was the three-dimensional stacking pattern of the blade sections, which would naturally lead to spanwise variations in the

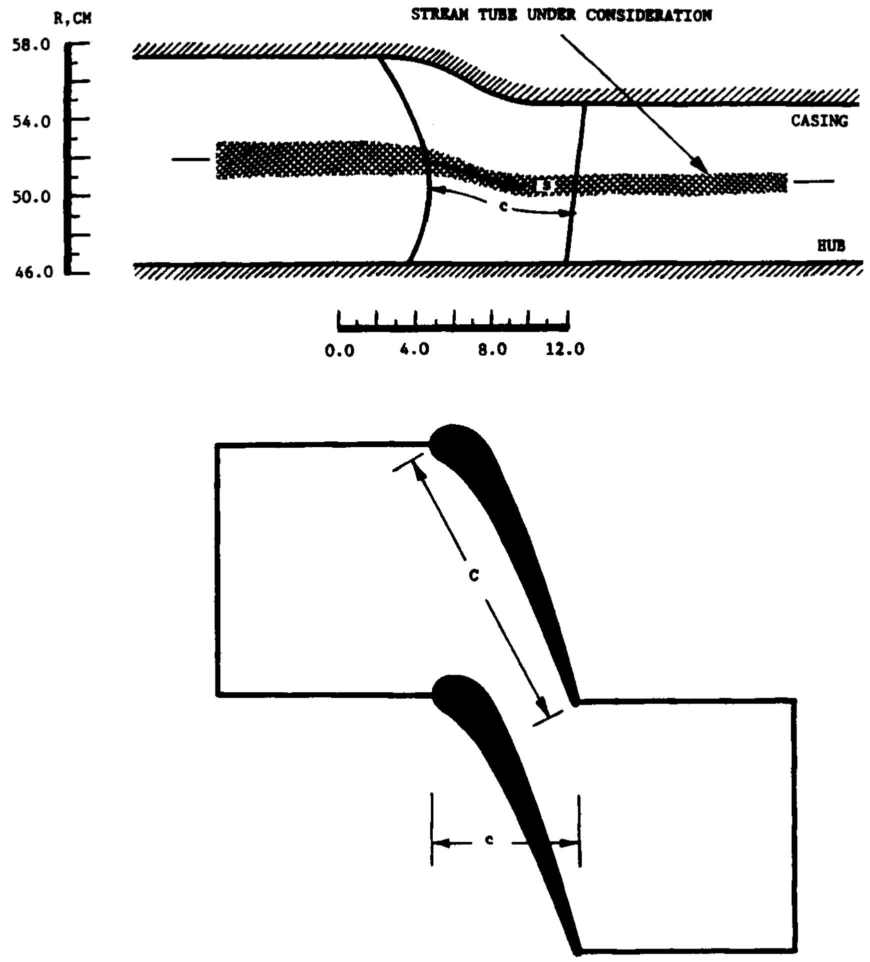

Figure 6. Meridonal and blade-to-blade views of the low-aspect-ratio stator[19]

velocity components that in turn create two significant shear stress components on the inner and outer surfaces of the stream tube (Figure 2). In fact, the choice of this stator section has provided an environment within which all terms of the flow-governing equations, particularly the newly introduced ones, were of significant contribution. Furthermore, since these terms are commonly functions of the distance s in the direction of the meridional streamline, it was necessary to provide a sufficient number of grid lines in this direction in the process of creating the finite element discretization model of the cascade unit as shown in Figure 7. The closeness of the grid lines in the finite element model is particularly observed around the trailing edge and in the near-wake region for better resolution of the high shear stresses in this flow-mixing region. This local refinement was necessary to offset the numerical consequences of not aligning grid lines with the yet unknown direction of the stagnation streamline.

Preparation of the stator input data was based on the aerofoil geometry and operating conditions provided by Waterman.[19,20] Of these, the latter set of data was not used to pre-establish the exit flow direction, as is the case in parabolized flow models, since this is naturally

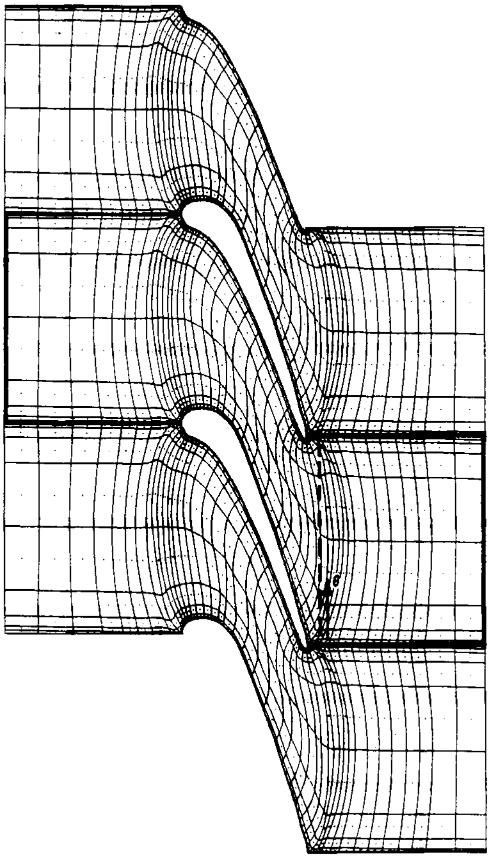

Figure 7. Finite element discretization model of the cascade unit as naturally connected to the two adjacent units

produced as part of the numerical solution. It did, however, aid in estimating the different derivatives of velocity components normal to the stream tube, which are responsible for the two shear stress components described earlier. Since these derivatives are presumed known functions of the meridional distance s (Figure 1), be that the outcome of a low-order axisymmetric flow analysis or experimental data, it was necessary to assume a 'reasonable' form of these functional relationships in terms of the spanwise velocity derivatives at the stator trailing edge, being the only location where such data were provided.

Referring to Figure 6, it was hypothesized that the spanwise velocity derivatives are, for the major part, created by the continuous flow turning within the blade-to-blade passage, coupled with the spanwise variation of the aerofoil setting angles. Furthermore, examination of the blade geometry revealed that the flow deflection in the passage is gradual and that the rate of this deflection is zero at both the leading and trailing edge stations. The blade three-dimensionality, on the other hand, was judged to have a minimum impact at these stations owing to the simple non-swirling flow behaviour at the leading edge and the small spanwise curvature of the blade surface near the trailing edge of this particular stator.[20] With these findings in mind, variation of the spanwise derivatives along the meridional flow trajectory was established using a single form of functional relationship as follows:

$$\Psi = \Psi_0\left[3\left(\frac{s}{C}\right)^2 - 2\left(\frac{s}{C}\right)^3\right], \quad 0 \leqslant \frac{s}{C} \leqslant 1{\cdot}0, \tag{14}$$

where s is the distance, measured from the leading edge, along the meridional flow trajectory (Figure 1), Ψ stands for $\partial^2 V_s/\partial n^2$, $\partial V_\theta/\partial n$ or $\partial^2 V_\theta/\partial n^2$ (see Appendix), Ψ_0 refers to the value of Ψ at the trailing edge and C is the aerofoil true chord (Figure 6).

Note that the above is a third-order polynomial with zero s-derivatives at the leading and trailing edges. The trailing edge values Ψ_0 appearing in this expression represent the minimum amount of data that is typically known to the designer at the preliminary design phase, which is when the velocity diagrams at several spanwise locations are established. It is again emphasized that introducing such derivatives in this type of cascade flow problem is unprecedented.

Numerical results of the stator flow analysis are compared with a set of experimental data and a three-dimensional parabolized flow solution[19,20] for a Reynolds number (based on the true aerofoil chord C) of $2{\cdot}58 \times 10^5$. Although this number may theoretically place the stator flow field slightly inside the turbulent flow range, there is actually no evidence, in view of the favorable pressure gradient magnitude and the reportedly negligible free stream turbulence,[20] that this was the case. In fact, results of the boundary layer computations for this stator, based on the experimental aerodynamic loading in Reference 20, imply that the likelihood of boundary layer transition from laminar to turbulent would be very much confined to a small segment near the trailing edge on the blade suction side. The stator flow during testing was otherwise laminar for all practical purposes.

The stator flow computations were terminated at a Reynolds number of 2000. While it is theoretically true that a substantial increase in this number was indeed feasible (up to roughly 10 000), the strong non-linearity of the flow-governing equations in this case would have caused the iterative process to be both slow and costly. On the other hand, a modest elevation of the Reynolds number, judging by the history of the computed flow variables during the solution process, would not have had the substantial numerical effects that would alter the major conclusions of this study.

Figure 8 shows a comparison of the blade aerodynamic loading between the current flow model and the data mentioned earlier. The horizontal axis in this figure is the non-dimensional distance s in the direction of the meridional streamline, and the vertical axis is the local static-to-inlet total pressure ratio. As seen, the agreement between the current results and the flow measurements is good where experimental data points are given. Note that verification of the results over the front 40% of the blade suction side is not possible owing to the lack of experimental data in this region. However, examination of the more detailed experimental loading[20] for the hub and casing sections of the same blade revealed loading details similar to that detected by the current model at the midspan section, including in particular the local diffusion over the suction side. Knowing that the aerofoil sections at all three locations are characteristically similar, it is perhaps reasonable to assume that the computed pressure, even in this region, is in good standing. In fact, it is clear in Figure 8 that the computed pressure distribution over the major part of the blade surface is closer to the flow measurements than that of the fully three-dimensional flow solution[20] based on a parabolic flow assumption. This includes, in particular, the trailing edge region where prior selection of the flow exit angle, which is tied to the flow parabolization, is most damaging.

Figure 8 also illustrates the effect of including the new terms in the flow-governing equations. As explained earlier, the single most significant group of such terms includes the shear stress

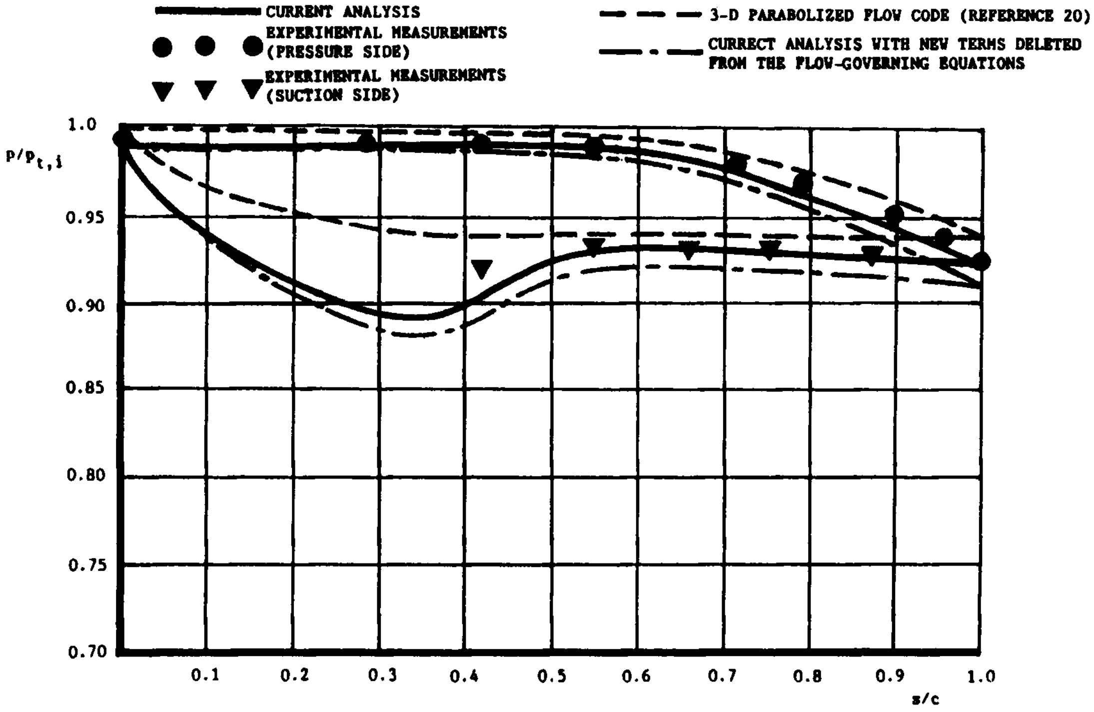

Figure 8. Non-dimensional static pressure distribution over the blade pressure and suction sides

components on the inner and outer surfaces of the stream tube (Figure 2). The program was consistently re-executed with the only difference being that of extracting these shear components in an attempt to assess their influence on the flow solution. It is important to point out that the effect of these stress components would be most significant in the rear segment of the blade (equation (14)). With this in mind, examination of Figure 8 reveals that the aerodynamic loading, particularly in the rear blade segment, is worsened as these new terms are deleted.

Shown in Figure 9 is a comparison of the computed exit angle distribution with the experimental measurements. Both sets of data in this figure correspond to the dotted line in Figure 7 and the flow angle is measured from the through-flow direction. Recalling the significant difference in Reynolds number between the two data sets, and that this would primarily affect the viscous region near the blade surface, it is sensible to see the computed angle in Figure 9 deviating the most near the two trailing edges in the blade-to-blade passage. However, the fact that the average exit angle in this Figure differs by only 2·1% from the experimental value is definitely encouraging. Note that comparison of the current exit angle distribution and that of the parabolized flow code is invalid, since the exit angle in the latter code is essentially fixed owing to the duct-like flow field to which the problem is reduced in this case.

Figure 10 shows a vector plot of velocity in the region downstream from the blade trailing edge. This is a critical region of the flow domain where a major part of the overall total pressure loss occurs owing to boundary layer mixing. Knowledge of the wake structure and extent in this region is of particular interest as a basis for optimizing the stator/rotor gap length within a turbomachinery stage in an attempt to suppress the time-dependent interaction effects between the stationary and rotating blade rows.

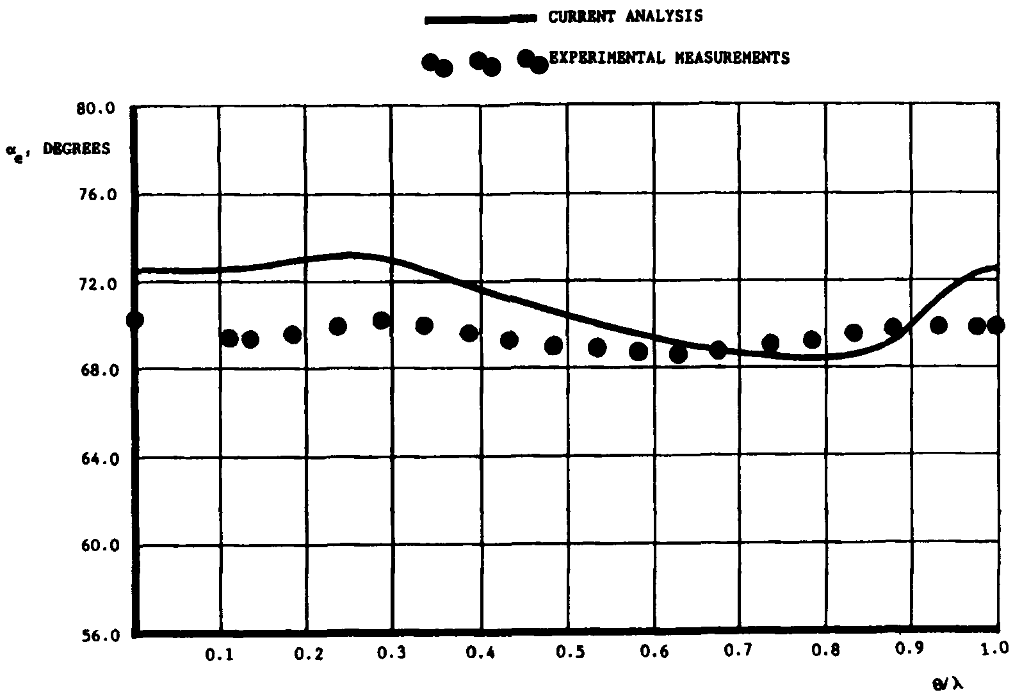

Figure 9. Circumferential variation of the flow exit angle

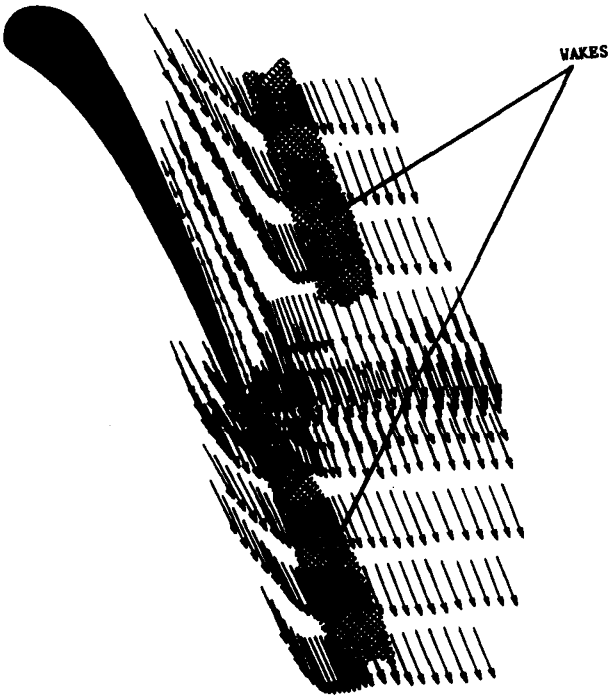

Figure 10. Vector plot of the velocity field in the boundary-layer-mixing region

4. CONCLUSIONS

An expanded model of the blade-to-blade quasi-three-dimensional cascade flow problem has been developed. The primary and foremost contribution of this model lies in introducing significant terms in the flow-governing equations in such a way as to restore the mutual interaction between the flow field in the blade-to-blade passage and that in the hub-to-casing meridional plane. Of these, terms proportional to the shear stresses over the stream tube inner and outer surfaces are representative of a group that is categorically unprecedented. Verification of the model was successfully achieved using existing flow measurements that correspond to the midspan section of a low-aspect-ratio stator. The blade aerodynamic loading was also compared with the loading obtained through a three-dimensional parabolized flow approach. The confirmed drawbacks of the latter approach, including inaccurate flow exit conditions and circulation magnitude, are indeed typical and, to a varied extent, apply to the currently existing and widely used models in which ellipticity of the viscous flow field is not rigorously introduced.

ACKNOWLEDGEMENT

This study was funded by the Turbomachinery Research Consortium, Texas A&M University.

APPENDIX: DERIVATION OF THE FLOW-GOVERNING EQUATIONS

Referring to the velocity and stress patterns associated with the fluid element in Figure 2 and denoting the direction normal to the stream tube by n, the continuity and momentum equations can be expressed as follows.

continuity equation

$$\frac{1}{b}\frac{\partial}{\partial s}(rbV_s)+\frac{\partial V_\theta}{\partial \theta}=0. \tag{15}$$

s-momentum equation

$$\begin{aligned}
&\rho\left(b+\frac{\mathrm{d}b}{2}\right)\left(r+\frac{\mathrm{d}r}{2}\right)\mathrm{d}s\mathrm{d}\theta\left(V_s\frac{\partial V_s}{\partial s}+\frac{V_\theta}{r}\frac{\partial V_s}{\partial \theta}-\frac{V_\theta^2}{r}\frac{\mathrm{d}r}{\mathrm{d}s}\right)\\
&\quad=\left(p+\frac{\partial p}{\partial s}\mathrm{d}s\right)(b+\mathrm{d}b)(r+\mathrm{d}r)\mathrm{d}\theta+pbr\mathrm{d}\theta+\left(\sigma_s+\frac{\partial \sigma_s}{\partial s}\mathrm{d}s\right)(b+\mathrm{d}b)(r+\mathrm{d}r)\mathrm{d}\theta-\sigma_s br\mathrm{d}\theta\\
&\qquad+\left(\tau_{\theta s}+\frac{\partial \tau_{\theta s}}{\partial \theta}\mathrm{d}\theta\right)\left(b+\frac{\mathrm{d}b}{2}\right)\mathrm{d}s-\tau_{\theta s}\left(b+\frac{\mathrm{d}b}{2}\right)\mathrm{d}s+\left[\tau_{ns}+\frac{\partial \tau_{ns}}{\partial n}\left(b+\frac{\mathrm{d}b}{2}\right)\right]\mathrm{d}A_\mathrm{o}-\tau_{ns}\mathrm{d}A_\mathrm{i},
\end{aligned} \tag{16}$$

where $\mathrm{d}A_\mathrm{i}$ and $\mathrm{d}A_\mathrm{o}$ are the inner and outer areas of the differential control volume in Figure 2. These infinitesimally small surface areas can be expressed as follows:

$$\mathrm{d}A_\mathrm{i}=\mathrm{d}s\left(r+\frac{\mathrm{d}r}{2}\right)\mathrm{d}\theta, \tag{17}$$

$$\mathrm{d}A_\mathrm{o}=\left(\mathrm{d}s-\frac{b\mathrm{d}s}{R_\mathrm{m}}-\frac{1}{2R_\mathrm{m}}\mathrm{d}b\mathrm{d}s\right)\left(r+\frac{\mathrm{d}r}{2}+b\cos\phi+\frac{\mathrm{d}b}{2}\cos\phi\right)\mathrm{d}\theta, \tag{18}$$

where R_m is the radius of curvature of the stream tube in the meridional (z–r) plane and ϕ is the slope angle of the stream tube with respect to the positive axial direction. Referring to Figure 2, the following relationship also applies:

$$\cos\phi = \mathrm{d}r/\mathrm{d}s. \tag{19}$$

θ-momentum equation

$$\begin{aligned}
&\rho\left(b+\frac{\mathrm{d}b}{2}\right)\left(r+\frac{\mathrm{d}r}{2}\right)\mathrm{d}s\mathrm{d}\theta\left(V_s\frac{\partial V_\theta}{\partial s}+\frac{V_\theta}{r}\frac{\partial V_\theta}{\partial \theta}-\frac{V_sV_\theta}{r}\frac{\mathrm{d}r}{\mathrm{d}s}\right)\\
&\quad=-\left(p+\frac{\partial p}{\partial\theta}\mathrm{d}\theta\right)\left(b+\frac{\mathrm{d}b}{2}\right)\mathrm{d}s+p\left(b+\frac{\mathrm{d}b}{2}\right)\mathrm{d}s+\left(\sigma_\theta+\frac{\partial\sigma_\theta}{\partial\theta}\mathrm{d}\theta\right)\left(b+\frac{\mathrm{d}b}{2}\right)\mathrm{d}s-\sigma_\theta\left(b+\frac{\mathrm{d}b}{2}\right)\mathrm{d}s\\
&\qquad+\left(\tau_{s\theta}+\frac{\partial\tau_{s\theta}}{\partial s}\mathrm{d}s\right)(b+\mathrm{d}b)(r+\mathrm{d}r)\mathrm{d}\theta-\tau_{s\theta}br\mathrm{d}\theta+\left[\tau_{n\theta}+\frac{\partial\tau_{n\theta}}{\partial n}\left(b+\frac{\mathrm{d}b}{2}\right)\right]\mathrm{d}A_\mathrm{o}-\tau_{n\theta}\mathrm{d}A_\mathrm{i},
\end{aligned}\tag{20}$$

where $\mathrm{d}A_\mathrm{i}$ and $\mathrm{d}A_\mathrm{o}$ are the same as in expressions (17) and (18) above. Substituting expressions (17)–(19) in equations (16) and (20), dividing by $rb\mathrm{d}s\mathrm{d}\theta$ and ignoring high-order terms, the momentum equations can be rewritten as follows:

$$\begin{aligned}
&\rho\left(V_s\frac{\partial V_s}{\partial s}+\frac{V_\theta}{r}\frac{\partial V_s}{\partial\theta}-\frac{V_\theta^2}{r}\frac{\mathrm{d}r}{\mathrm{d}s}\right)\\
&\quad=-\frac{\partial p}{\partial s}-\left(\frac{1}{b}\frac{\mathrm{d}b}{\mathrm{d}s}+\frac{1}{r}\frac{\mathrm{d}r}{\mathrm{d}s}\right)p+\frac{\partial\sigma_s}{\partial s}+\left(\frac{1}{b}\frac{\mathrm{d}b}{\mathrm{d}s}+\frac{1}{r}\frac{\mathrm{d}r}{\mathrm{d}s}\right)\sigma_s+\frac{1}{r}\frac{\partial\tau_{\theta s}}{\partial\theta}+\frac{\partial\tau_{ns}}{\partial n}+\frac{1}{r}\left(\frac{\mathrm{d}r}{\mathrm{d}s}-\frac{r}{R_\mathrm{m}}\right)\tau_{ns},
\end{aligned}\tag{21}$$

$$\begin{aligned}
&\rho\left(V_s\frac{\partial V_\theta}{\partial s}+\frac{V_\theta}{r}\frac{\partial V_\theta}{\partial\theta}-\frac{V_sV_\theta}{r}\frac{\mathrm{d}r}{\mathrm{d}s}\right)\\
&\quad=-\frac{1}{r}\frac{\partial p}{\partial\theta}+\frac{1}{r}\frac{\partial\sigma_\theta}{\partial\theta}+\frac{\partial\tau_{s\theta}}{\partial s}+\left(\frac{1}{b}\frac{\mathrm{d}b}{\mathrm{d}s}+\frac{1}{r}\frac{\mathrm{d}r}{\mathrm{d}s}\right)\tau_{s\theta}+\frac{\partial\tau_{n\theta}}{\partial n}+\frac{1}{r}\left(\frac{\mathrm{d}r}{\mathrm{d}s}-\frac{r}{R_\mathrm{m}}\right)\tau_{n\theta}.
\end{aligned}\tag{22}$$

Note that the radius of curvature R_m (Figure 2), appearing in the last two terms of equations (21) and (22), would be infinite in the case of a purely axial turbomachine. In this case the derivative $\mathrm{d}r/\mathrm{d}s$ would vanish along the stream tube. Both of these conditions are met with a reasonable accuracy in axial flow turbomachines where the meridional flow trajectory (Figure 2) is predominantly in the axial direction.

Assuming a Newtonian fluid, the stress/strain relations expressed in the curvilinear frame of reference (Figure 2) are as follows:

$$\begin{aligned}
\sigma_s&=2\mu\frac{\partial V_s}{\partial s},\\
\sigma_\theta&=2\mu\left(\frac{1}{r}\frac{\partial V_\theta}{\partial\theta}+\frac{V_s}{r}\frac{\mathrm{d}r}{\mathrm{d}s}\right),\\
\tau_{s\theta}=\tau_{\theta s}&=\mu\left(\frac{1}{r}\frac{\partial V_s}{\partial\theta}+\frac{\partial V_\theta}{\partial s}-\frac{V_\theta}{r}\frac{\mathrm{d}r}{\mathrm{d}s}\right),\\
\tau_{ns}&=\mu\frac{\partial V_s}{\partial n},\\
\tau_{n\theta}&=\mu\left(\frac{1}{r}\frac{\partial V_\theta}{\partial n}-\frac{V_\theta}{r^2}\right),
\end{aligned}$$

where μ is the viscosity coefficient. Substitution of the preceding relations in the momentum equations (21) and (22) gives rise to the final set of linearized momentum equations, which can be expressed in terms of the kinematic viscosity coefficient ν as follows:

$$\nu\nabla^2 V_s = \frac{1}{\rho}\left(\frac{1}{b}\frac{\mathrm{d}b}{\mathrm{d}s}+\frac{1}{r}\frac{\mathrm{d}r}{\mathrm{d}s}\right)p+\frac{1}{\rho}\frac{\partial p}{\partial s}+\alpha_1\frac{\partial V_s}{\partial s}+\alpha_2\frac{\partial V_s}{\partial\theta}+\alpha_3 V_s+\alpha_4 V_\theta+\alpha_5, \tag{23}$$

$$\nu\nabla^2 V_\theta = \frac{1}{\rho r}\frac{\partial p}{\partial\theta}+\beta_1\frac{\partial V_\theta}{\partial s}+\beta_2\frac{\partial V_\theta}{\partial\theta}+\beta_3 V_\theta+\beta_4\frac{\partial V_s}{\partial\theta}+\beta_5 V_s+\beta_6, \tag{24}$$

where

$$\alpha_1 = \hat{V}_s-\nu\left(\frac{1}{b}\frac{\mathrm{d}b}{\mathrm{d}s}\right),$$

$$\alpha_2 = \hat{V}_\theta/r,$$

$$\alpha_3 = \nu\frac{\mathrm{d}}{\mathrm{d}s}\left(\frac{1}{b}\frac{\mathrm{d}b}{\mathrm{d}s}+\frac{1}{r}\frac{\mathrm{d}r}{\mathrm{d}s}\right),$$

$$\alpha_4 = -\frac{\hat{V}_\theta}{r}\frac{\mathrm{d}r}{\mathrm{d}s},$$

$$\alpha_5 = -\nu\frac{\partial^2 V_s}{\partial n^2}-\frac{\nu}{r}\left(\frac{\mathrm{d}r}{\mathrm{d}s}-\frac{r}{R_\mathrm{m}}\right)\frac{\partial V_s}{\partial n},$$

$$\beta_1 = \hat{V}_s-\nu\left(\frac{1}{b}\frac{\mathrm{d}b}{\mathrm{d}s}-\frac{1}{r}\frac{\mathrm{d}r}{\mathrm{d}s}\right),$$

$$\beta_2 = \hat{V}_\theta/r,$$

$$\beta_3 = -\frac{\hat{V}_s}{r}\frac{\mathrm{d}r}{\mathrm{d}s}+\nu\left(\frac{1}{br}\frac{\mathrm{d}b}{\mathrm{d}s}\frac{\mathrm{d}r}{\mathrm{d}s}+\frac{1}{r}\frac{\mathrm{d}^2r}{\mathrm{d}s^2}\right),$$

$$\beta_4 = -\frac{\nu}{r^2}\frac{\mathrm{d}r}{\mathrm{d}s},$$

$$\beta_5 = 0,$$

$$\beta_6 = -\frac{\nu}{r}\frac{\partial^2 V_\theta}{\partial n^2}+\frac{\nu}{r^2}\frac{\partial V_\theta}{\partial n}-\frac{\nu}{r}\left(\frac{\mathrm{d}r}{\mathrm{d}s}-\frac{r}{R_\mathrm{m}}\right)\left(\frac{1}{r}\frac{\partial V_\theta}{\partial n}-\frac{V_\theta}{r^2}\right),$$

with the symbol ($\hat{}$) signifying a value that is known from a previous iteration or an initial guess, and ρ being the fluid density.

In deriving equations (23) and (24), expressions derived from the continuity equation (15), by differentiating both sides of this equation with respect to s and θ, were utilized. Also used in the process was the expression of the Laplacian operator in the current frame of reference (Figure 2) as follows:

$$\nabla^2 = \frac{\partial}{\partial s^2}+\frac{1}{r^2}\frac{\partial^2}{\partial\theta^2}+\frac{1}{r}\frac{\mathrm{d}r}{\mathrm{d}s}\frac{\partial}{\partial s}.$$

As seen, the free terms α_5 and β_6 above are proportional to the lateral velocity gradients and are numerically treated as source terms.

The preceding equations describe the flow pattern in a stationary frame of reference for a non-rotating aerofoil cascade. Expansion of the equations to a rotating cascade can simply be achieved by replacing the absolute velocity $\vec{V}$ by the relative velocity $\vec{W}$ and including the centrifugal and Coriolis acceleration components in the momentum equations. In doing this, constraints involving $\vec{V}$ can easily be written in terms of $\vec{W}$ by recalling that

$$\vec{W} = \vec{V} - \omega r \vec{e}_\theta,$$

with ω being the rotational speed. The final set of equations in this case are identical to equations (15), (23) and (24), with the exception that the coefficients α_4, α_5 and β_5 are now defined as follows:

$$\alpha_4 = -\frac{\hat{W}_\theta}{r}\frac{\mathrm{d}r}{\mathrm{d}s} - 2\omega\frac{\mathrm{d}r}{\mathrm{d}s},$$

$$\alpha_5 = -\nu\frac{\partial^2 W_s}{\partial n^2} - \omega^2 r\frac{\mathrm{d}r}{\mathrm{d}s},$$

$$\beta_5 = 2\omega\frac{\mathrm{d}r}{\mathrm{d}s}.$$

REFERENCES

1. E. Baskharone and A. Hamed, 'A new approach in cascade flow analysis using the finite element method', *AIAA J.*, **19**, 65–71 (1981).
2. E. R. McFarland, 'A rapid blade-to-blade solution for use in turbomachinery design', *J. Eng. Gas Turbines Power, ASME Trans.*, **106**, 376–382 (1984).
3. M. Koya and S. Kotake, 'Numerical analysis of the fully three-dimensional periodic flows through a turbine stage', *ASME Paper 85-GT-57*, March 1985.
4. M. M. Rai, 'Navier–Stokes simulation of rotor–stator interaction using patched and overlaid grids', *AIAA Paper 85-1519*, July 1985.
5. R. L. Davis, R. H. Ni and J. E. Carter, 'Cascade viscous flow analysis using the Navier–Stokes equations', *AIAA J. Propulsion*, **3**, 406–414 (1987).
6. R. V. Chima, 'Explicit multigrid algorithm for quasi-three-dimensional viscous flows in turbomachinery', *AIAA J. Propulsion*, **3**, 397–405 (1987).
7. R. V. Chima, 'Inviscid and viscous flows in cascades with an explicit multiple-grid algorithm', *AIAA J.*, **23**, 1556–1563 (1985).
8. C. Hah, 'A Navier–Stokes analysis of three-dimensional turbulent flows inside turbine blade rows at design and off-design conditions', *J. Eng. Gas Turbines Power, ASME Trans.*, **106**, 421–429 (1984).
9. K. R. Kirtley and B. Lakshminarayana, 'Computation of three-dimensional turbomachinery flows using a coupled parabolic marching method', *ASME Paper 88-GT-80*, 1988.
10. W. N. Dawes, 'Development of a 3D Navier Stokes solver for application to all types of turbomachinery', *ASME Paper 88-GT-70*, 1988.
11. C. H. Wu, 'A general theory of three-dimensional flow in subsonic and supersonic turbomachines of the axial-, radial- and mixed-flow types', *NACA TN 2604*, January 1952.
12. C. Hirsch and G. Warzee, 'A finite element method for through flow calculations in turbomachines', *J. Fluids Eng., ASME Trans.*, **98**, 403–421 (1976).
13. M. R. Vanco, 'Fortran program for calculating velocities in the meridional plane of a turbomachine: I—Centrifugal compressor', *NASA TN D-6701*, March 1972.
14. J. Hourmouziadis and N. Hubner, '3-D design of turbine airfoils', *ASME Paper 85-GT-188*, March 1985.
15. P. S. Huyakorn, C. Taylor, R. L. Lee and P. M. Gresho, 'A comparison of various mixed-interpolation finite elements in the velocity–pressure formulation of the Navier–Stokes equations', *J. Comput. Fluids*, **6**, 25–35 (1978).
16. G. F. Carey and J. T. Oden, *Finite Elements: Fluid Mechanics, The Texas Finite Element Series, Vol. VI*, Prentice-Hall, Englewood Cliffs, NJ, 1986.
17. A. J. Baker, *Finite Element Computational Fluid Mechanics*, Hemisphere, New York, 1983.
18. S. K. Gupta and K. K. Tanji, 'Computer program for solution of large, sparse, unsymmetric systems of linear equations', *Int. j. numer. methods eng.*, **11**, 1251–1259 (1977).
19. W. F. Waterman and W. A. Tall, 'Measurement and prediction of 3-D viscous flows in low-aspect-ratio turbine nozzles', *ASME Paper 76-GT-73*, 1976.
20. W. F. Waterman, 'Low-aspect-ratio turbine technology—Final report for phase I', *AiResearch Report 75-21701* (2), August 1975.